Fuel 417 (2026) 138559

Contents lists available at ScienceDirect

Fuel

journal homepage: www.elsevier.com/locate/fuel

Full Length Article

Pore structure evolution in organic-rich shale during thermal maturation: Insights from hydrous pyrolysis of two lacustrine kerogens

Fengtian Bai [a,b], Lee A. Stevens [b], Clement N. Uguna [b], Wei Li [b], Will Meredith [b], Colin E. Snape [b], Christopher H. Vane [c], Yumin Liu [b,d], Chenggong Sun [b,e,*]

[a] State Key Laboratory of Deep Earth Exploration and Imaging, College of Construction Engineering, Jilin University, Changchun 130061, Jilin, PR China
[b] Faculty of Engineering, University of Nottingham, Nottingham NG7 2TU, UK
[c] Organic Geochemistry Facility, British Geological Survey, Keyworth, Nottingham NG12 5GG, UK
[d] College of Earth Science, Jilin University, Changchun 130061, Jilin, PR China
[e] School of Chemical Engineering, University of Birmingham, Birmingham B15 2TT, UK

ARTICLE INFO

Keywords:
Lacustrine kerogen
High-pressure pyrolysis
Water pressure
Pore structure
Maturation
Minerals

ABSTRACT

Accurately predicting the evolution of pore networks under realistic thermo-hydro-mechanical conditions remains a critical challenge, limiting the reliable identification of hydrocarbon "sweet spots" in mature shale basins. This study aims to decouple the synergistic controls of thermal maturity, shale composition, water, and pressure on pore development. We conducted systematic, sequential high-pressure hydrous pyrolysis experiments on two compositionally distinct lacustrine shales, immature Huadian (Type II kerogen, high TOC, illite–smectite mixed-layer clay-rich) and Fushun (Type I kerogen, low TOC, siderite-rich) shales. Integrated geochemical analyses (vitrinite reflectance, Rock-Eval pyrolysis, TOC) and pore structure characterization (low-pressure N_2/CO_2 adsorption, SEM) revealed that thermal maturity is the primary driver for pore development, but its expression is fundamentally mediated by composition. Kerogen type dictates the evolutionary pathway, and TOC dominates the porosity magnitude. Minerals further modulate pore evolution, with carbonate dissolution regenerating porosity and clay stability determining pore integrity. Water is the most critical environmental factor, enhancing porosity by facilitating hydrocarbon expulsion, inhibiting pore-filling, and promoting mineral dissolution. Pressure exerts a dual role, with internal pore pressure promoting porosity, outweighing external compaction in our closed system. Notably, water pressure results in an additional 1.9–4.5-fold increase in pore volume during the wet gas cracking stage compared to non-hydrous conditions. These results establish a novel, integrated shale-water-pressure framework that advances beyond traditional maturity-centric models by quantitatively distinguishing the roles of and interactions between key controlling factors, providing a mechanistic basis for predicting reservoir quality, although its field application requires calibration to account for basin-specific geological complexity.

1. Introduction

Nanopore networks serve as the foundational architecture governing hydrocarbon storage and transport in shale reservoirs, with significant implications for improving shale oil and gas recovery and ensuring the stability of geological CO_2 storage [1–4]. Given the global importance of unconventional hydrocarbon resources, accurately predicting the evolution of these nanopores under realistic geological conditions has emerged as a key research priority [5,6].

Extensive research has focused on the effects of organic matter thermal maturation, hydrocarbon generation, and inorganic diagenesis on pore structure development in organic-rich source rocks [7–11]. Results showed that the development of organic pores in shale is influenced by multiple factors, such as the kerogen type, total organic carbon (TOC) content, and thermal maturity [12,13]. As maturity increases, kerogen generates substantial bitumen, within which nanoscale pores develop during subsequent cracking [14]. The interaction between hydrocarbons and pore networks determines whether pores are preserved or occluded across maturation stages [15,16]. Concurrently, inorganic pores, particularly those associated with clay minerals, represent an

* Corresponding author at: School of Chemical Engineering, University of Birmingham, Birmingham B15 2TT, UK.
E-mail address: c.sun.2@bham.ac.uk (C. Sun).

https://doi.org/10.1016/j.fuel.2026.138559
Received 25 September 2025; Received in revised form 19 December 2025; Accepted 27 January 2026
Available online 4 February 2026

essential component of shale pore system [17–19]. Mineral transformation occurs alongside organic matter pyrolysis, contributing to pore development [20]. Acidic fluids generated during organic matter decomposition can react with minerals, leading to processes such as calcite dissolution [21]. A reduction of feldspar in minerals with increased pyrolysis temperature in a CO_2-steam pyrolysis condition was reported by Wan et al. [22].

Despite considerable research, the complex interplay of multiple controlling factors under realistic thermo-hydro-mechanical conditions remains inadequately quantified. A critical knowledge gap persists in understanding the synergistic effects of thermal maturity, organic matter, minerals, water, and pressure regimes during thermo-hydro-mechanical processes. The role of pressure is particularly debated, with reported impacts on porosity ranging from negligible [23–25] to enhancing [26–29] to inhibitory [30–33]. This paradox stems from the dual function of pressure, which can preserve pores through internal overpressure generated during hydrocarbon cracking [34,35], while simultaneously reducing porosity via external mechanical compaction [10,15,36]. The effect is strongly lithology-dependent and varies across different pore size ranges [34,37]. Simultaneously, water is increasingly recognized not merely as a reaction medium but as an active geochemical agent that critically influences hydrocarbon generation kinetics, expulsion efficiency, and fluid phase behavior [22,38], thereby introducing considerable complexity to pore evolution [39,40]. Comparative studies indicate that hydrous pyrolysis generally enhances total pore volume and modifies pore geometry compared to anhydrous conditions, promoting better connectivity for fluid expulsion [38,41]. This porosity-enhancing effect is therefore integral to models that couple hydrocarbon generation with diagenesis [41]. Quantifying these intertwined effects, particularly the net impact of water and pressure, is especially urgent for evaluating overpressured basins, where pore-fluid pressures significantly exceed hydrostatic conditions [42]. Bridging this knowledge gap is essential for advancing the predictive assessment of shale reservoir quality.

To address this issue, the present study employs sequential pyrolysis experiments under controlled hydrostatic pressure on immature Huadian (HD) and Fushun (FS) shales, with a comparative analysis of non-hydrous and hydrous conditions. Integrated geochemical (vitrinite reflectance, Rock-Eval pyrolysis, TOC) and pore structural analyses (low-pressure N_2/CO_2 sorption, SEM) were applied to trace nanopore evolution across thermal maturity stages. By decoupling the effects of thermal maturity, shale composition, water, and pressure, this work aims to elucidate the governing mechanisms of porosity evolution in organic-rich shales, with implications for predicting "sweet spots" in mature to overmature shale basins and improving the economic sustainability of shale resource exploitation.

2. Materials and methods

2.1. Sample

The immature, organic-rich shale samples in this study were collected from the HD Basin and FS Basin in China. General characteristics of these samples have been reported previously [43]. Mineralogical composition, determined by X-ray diffraction, shows that HD shale is rich in calcite (9%) and illite–smectite (I/S) mixed-layer clay (39.8%), whereas FS shale is predominantly composed of siderite (12.6%) and kaolinite (32.4%, Table S1). Prior to experiments, the samples were

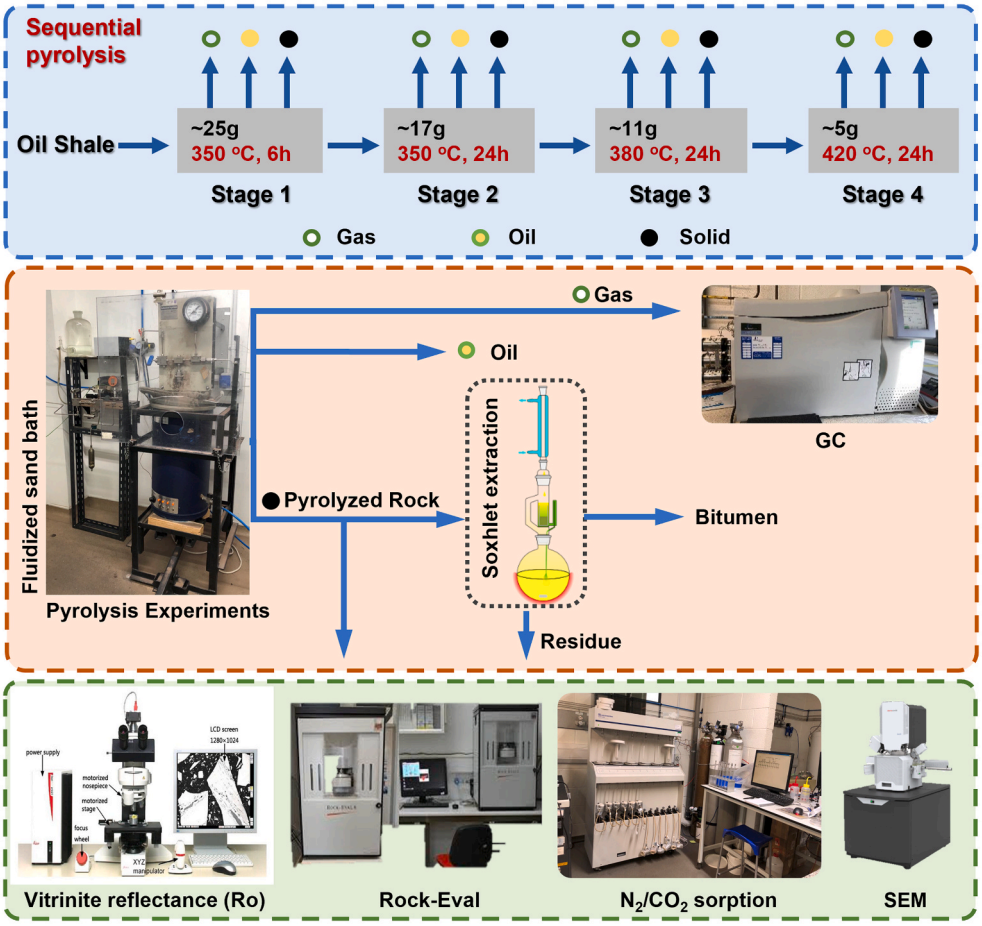

Fig. 1. Schematic diagram of the experimental setup and product analysis methods.

crushed into 2–5 mm chips and homogenized through thorough mixing.

2.2. High-pressure water pyrolysis experiments

The experimental procedure, as described in previous studies [43–46], is summarized as follows (Fig. 1).

Sequential pyrolysis experiments were conducted under non-hydrous pyrolysis (NP), low-water pressure (LP) of 16–39 MPa, and high-water pressure (HP) of 50–60 MPa in a 25 ml Hastelloy cylindrical pressure vessel. Heat was applied using a fluidized sand bath, connected to a compressed air source and regulated by an external temperature controller. Prior to each experiment, the sand bath was preheated to the target temperature and allowed to stabilize.

For all runs, the vessel was loaded with the sample and deionized water (for runs of LP and HP). The system was then flushed with nitrogen gas to remove air and pressurized with nitrogen to 0.2 MPa to maintain an inert atmosphere. In LP experiments, 15 ml of water was added before heating to generate pressure through thermal expansion and hydrocarbon generation. The resulting pressure varied between 16 MPa and 39 MPa during each run (Table S2), influenced by temperature, TOC content, gas generation, and the sample maturity. For HP experiments, 20 ml of water was initially introduced. After placing the vessel into the preheated sand bath and allowing the pressure to stabilize, additional water was injected via an external compression system to achieve an initial pressure of 50 MPa. Overpressures (up to 60.5 MPa) observed in some HP runs were attributed to thermal expansion of injected water and in-situ hydrocarbon gas generation.

Each sequential experiment was started using 25 g of the shale sample and subjected to a multi-stage heating sequence: Stage 1 at 350 °C for 6 h, followed by Stages 2–4 under the same pyrolysis conditions at 350 °C for 24 h, 380 °C for 24 h, and 420 °C for 24 h, respectively. After each run, the system was cooled to ambient temperature, and gases and expelled oil were collected. The pyrolyzed rocks were dried, and approximately 5 g was subsampled for analysis. The remaining rocks were used in the subsequent pyrolysis stage. The high temperatures (350–420 °C) were intentionally selected to accelerate the million-year natural maturation processes into a tractable 24 h experimental timeframe. Base on the water pressure–temperature (P-T) phase diagram (Fig. S1), Stage 3 (380 °C) and Stage 4 (420 °C) in both LP and HP experiments meet the thermodynamic requirements for supercritical water. By contrast, the aqueous system remained subcritical during Stage 1 and Stage 2, with both of sub- and supercritical water enhancing extractive efficiency and oil expulsion [39]. This sequential approach provided non-cumulative product yields reflective of the hydrocarbon generation potential at each maturity stage. A parallel replicate was conducted for each sample to ensure the reproducibility.

Collected gases were analyzed immediately using a Clarus 580 GC equipped with FID and TCD detectors held at 200 °C. Method parameters followed those described in [43,47]. Expelled oil was collected from the water surface and reactor walls using dichloromethane. Approximately 3 g of pyrolyzed rock was Soxhlet-extracted with a 200 ml dichloromethane/methanol mixture (93:7) for > 48 h to recover retained bitumen. Both expelled oil and bitumen were classified as liquid hydrocarbons.

2.3. Geochemical and pore structure analysis

Vitrinite reflectance (VR) measurements were performed on both the initial (non-extracted) and Soxhlet-extracted pyrolyzed rocks. The samples were embedded in epoxy resin and prepared according to standard protocols. Prior to analysis, the mounted samples were ground and polished with progressively finer silicon carbide papers and colloidal silica to achieve a smooth, scratch-free surface. This measurement was measured using a J&M TIDAS MSP 200 microscope under non-polarized light at a wavelength of 546 nm with oil immersion, in accordance with the Chinese standard SY/T 5124-2012.

Rock-Eval pyrolysis and TOC analyses [46] were conducted in duplicate on the initial, non-extracted pyrolyzed rocks, and bitumen-extracted residues from the sequential experiments, and the average values are reported in the manuscript. Rock-Eval pyrolysis was carried out using a Vinci Technologies Rock-Eval 6 standard instrument. Approximately 60 mg of finely crushed rock was heated under a N_2 atmosphere using an initial oven program of 300 °C for 3 min and then from 300 to 650 °C at the rate of 25 °C min^{-1}. The oxidation stage was achieved by heating at 300 °C for 1 min, ramping to 850 °C at 20 °C min^{-1}, and maintaining at 850 °C for 5 min. Hydrocarbons released during pyrolysis were detected using a flame ionization detector, while CO and CO_2 were quantified with an infrared (IR) cell.

Low-pressure gas sorption analyses were performed on both initial and non-extracted pyrolyzed rocks (2–4 mm particles) using a Micromeritics Surface Area and Porosity Analyzer (ASAP 2420) to characterize pore properties. Prior to analysis, approximately 2 g of each sample was degassed under high vacuum (<1.3 Pa) at 120 °C for 48 h. N_2 sorption isotherms were measured at –196 °C (liquid nitrogen bath) across a relative pressure (P/P_0) range from 10^{-7} until 0.995, where P is the equilibrium pressure and P_0 is the saturation pressure. CO_2 sorption isotherms were conducted at 0 °C over a relative pressure range of 6×10^{-5} to 3.5×10^{-2}, corresponding to absolute pressures from 0.0002 MPa to 0.12 MPa, to specifically assess ultra-micropores (<0.8 nm) of samples [46,48]. Each sample was analyzed in duplicate, with consistent results (relative deviation < 5%) confirming the stability of the pore structure data.

The Brunauer-Emmett-Teller (BET) theory was applied to the N_2 adsorption data within the P/P_o range of 0.05–0.2 to determine the specific surface area, ensuring a positive BET 'C' parameter [49,50]. Non-local density functional theory equilibrium model assuming slit pores was applied to calculate the pore volume from 0.33 to 100 nm by combining N_2 and CO_2 adsorption isotherms [51–53].

The argon ion polishing scanning electron microscopy (SEM) experiment was performed on selected samples, where a Leica EM RES 102 ion milling system was used to fabricate a flat, damage-free surface via argon ion beam etching to eliminate mechanical polishing artifacts; subsequent high-resolution morphological and compositional characterization were conducted using a Thermo Apreo 2 SEM.

3. Results

The evolution of organic matter and the concomitant development of the pore network in HD and FS shales were systematically tracked across sequential pyrolysis stages. The geochemical characteristics of the initial samples are summarized in Table S2. Both source rocks were immature and oil-prone, with comparable initial maturities reflected by mean VR values of 0.42%Ro (HD) and 0.38%Ro (FS), but significantly different TOC contents and Rock-Eval results. The HD shale exhibited a high TOC content of 27.98%, with an S_1 value of 0.44 mg/g, an S_2 value of 175.58 mg/g, a hydrogen index (HI) of 628 mg HC/(g·TOC), and a T_{max} of 436 °C. In contrast, the FS shale had a lower TOC content of 8.79%, with an S_1 value of 0.91 mg/g, an S_2 value of 57.71 mg/g, a higher HI of 657 mg HC/(g·TOC), and the same T_{max} of 436 °C. Plots of HI versus T_{max} and S_2 versus TOC indicated that the HD shale contained Type II_1 kerogen, while the FS was dominated by Type I kerogen [54].

Through the four experimental stages, both shales underwent a continuous transition from immaturity to overmaturity, with pressure exerting minimal influence on the maturation pathway itself. Based on VR and Rock-Eval data, the evolution of organic matter can be divided into three distinct phases: Phase I (primary oil generation, mean VR < 1.0%Ro), which is represented by experimental Stages 1 and 2; Phase II (oil cracking, mean VR = 1.0–1.6%Ro), represented by Stage 3; and Phase III (wet gas cracking, mean VR > 1.6%Ro), represented by Stage 4. During Phase I, liquid hydrocarbon yields reached their maximum with limited gas hydrocarbon. Phase II saw a slight increase in gas yields and the onset of liquid hydrocarbon cracking, accompanied by pronounced

decreases in TOC, S_2, and HI values. In Phase III, gas generation increased markedly, accompanied by pronounced decreases in S_2 and HI values, with T_{max} of unextracted pyrolyzed rock soaring to 530–590 °C, indicating entry into a high to overmature stage.

Concurrent with the chemical transformation of organic matter, significant alterations in the nanopore structure were observed. The low-pressure N_2 isotherms revealed that both initial HD and FS shales exhibit Type IV(a) N_2 sorption isotherms with H2-type hysteresis (Fig. 2a), indicating complex pore structures containing ink-bottle and slit-like other irregular pores [50,55]. The distinct desorption plateau and cavitation between 0.4 and 0.5P/P_o suggest pore-blocking effects from narrow pore necks (<4 nm). Conversely, CO_2 adsorption isotherms conformed to Type I(b) (Fig. 2b), confirming microporous characteristics. HD shale demonstrated significantly greater adsorption capacities for both N_2 (5.0 vs. 0.5 cm^3/g) and CO_2 (2.8 vs. 0.4 cm^3/g) compared to FS shale, approximately 10 and 7 times higher, respectively, consistent with its higher total pore volume (0.0071 cm^3/g) and BET surface area (1.96 m^2/g, Table 1). Pore size distributions (PSDs) further illustrated multi-scale porosity spanning 0.3–0.45 nm, 10–60 nm, and > 90 nm, with comparable average pore diameters between the two shales (14.48 nm for HD and 14.34 nm for FS, Table 1).

Following pyrolysis, N_2 isotherms maintained their Type IV(a) shapes with hysteresis (Fig. 3), though significant morphological evolution occurred. The hysteresis loops shifted from H2 to H3 in HD samples under all conditions and in FS samples under NP (Fig. 3a–d), suggesting the development of slit-shaped pores, while FS samples under LP and HP conditions retained H2-type hysteresis (Fig. 3e–f). N_2 adsorption capacity generally increased with thermal maturity, with temporary reductions observed in early stages under NP conditions. Hydrous conditions (LP/HP) consistently enhanced N_2 adsorption compared to NP, with more pronounced pressure effects (LP to HP) in Stages 3–4 for HD shale and across all stages for FS shale (Fig. S2). CO_2 isotherms remained Type I(b) across all treatments, but CO_2 adsorption trends differed between shales (Fig. 3g-m). HD shale showed depressed capacities in Stages 1–3 relative to the initial sample, followed by a marked increase in Stage 4, while FS shale exhibited a general increasing trend from Stage 1, except under NP in Stage 1. Both shales displayed similar CO_2 adsorption capacities under hydrous conditions (LP and HP), which were consistently higher than those under NP (Fig. S3). This indicates that hydrous conditions promote ultra-micropore development, while increasing water pressure beyond LP level provides no further benefit.

PSD analysis of pyrolyzed samples (Fig. 4) revealed retention of principal pore features of initial shale in the ranges of 0.3–0.45 nm, 1–60 nm, and > 90 nm with additional developments. A distinct micropore peak at 0.37 nm was observed in all stages alongside an emerging peak at 1.68 nm in Stage 4 under LP/HP conditions, suggesting water-enhanced micropore formation. Mesopores (2–50 nm) developed considerably during thermal treatment, particularly within the 10–50 nm in Stages 3 and 4. Quantitative analysis of pore volumes (Table 1, Fig. S6) confirmed mesopores as the dominant contributors to total pore volume. HD shale exhibited distinct evolutionary patterns in which ultra-micropore and micropore volumes decreased initially before recovering at higher maturities, with this inflection delayed under hydrous conditions (Fig. S6a–b). In contrast, mesopore volume under LP and HP increased steadily from Stage 1, while NP conditions showed limited development until Stage 3 (Fig. S6c). FS shale demonstrated more gradual increases across all pore size ranges from Stage 1 to Stage 4 (Fig. S6f-S6j). Furthermore, macropores (50–70 nm and > 90 nm) also showed noticeable development.

Pressure exerted differential effects across a range of pore sizes. Micropore volume showed no consistent pressure dependence until Stage 4 and was even absent in some LP/HP samples (Stage 3, Figs. S4, S5, and S7), whereas meso- and macropores (>10 nm) responded strongly to water pressure. In HD shale, these pores increased markedly under LP/HP compared to NP, though increasing pressure from LP to HP in Stages 1 and 2 yielded no or negative additional gains (Fig. S4, S7). For instance, at Stage 4, incremental pore volume at 13 nm rose from ~ 0.0006 cm^3/g (NP) to 0.003 cm^3/g (LP), and 0.004 cm^3/g (HP), and the mesopore volume increased from 0.10 cm^3/g (LP) to 0.15 cm^3/g (HP), both significantly higher than the 0.03 cm^3/g under NP. FS shale showed consistent pore volume enhancement under LP/HP across all stages, with further augmentation from LP to HP throughout maturation (Fig. S5, S7), highlighting sample-specific responses to water pressure. The BET surface area growth correlated with increased mesopore volume during thermal maturation (Table 1 and Figs. S6–S7), underscoring the predominance of mesopores in surface area development.

The evolution of pore dimensions provided additional insights (Figs. S8, Table 1). Average pore diameters and window pore diameters generally increased initially, peaking at Stage 2, before decreasing during advanced maturation. The initial increase is attributed to thermal expansion, volatile release, and new pore formation, while the subsequent decrease results from extensive gas generation and mineral transformations promoting smaller secondary nanopores [15]. The final pore diameter of each sequence showed a decreased trend from NP to HP, which is due to the collapse of macropores and mesopores under high pressure [37]. The anomalous diameter decrease in Stage 2 under NP conditions reflects the competing effects of pore generation and infilling.

4. Discussion

Based on these findings, we establish that pore evolution is governed not merely by thermal maturity but by a critical interplay between shale compositions and hydro-mechanical conditions, where organic matter content and kerogen type define the primary porosity-generation

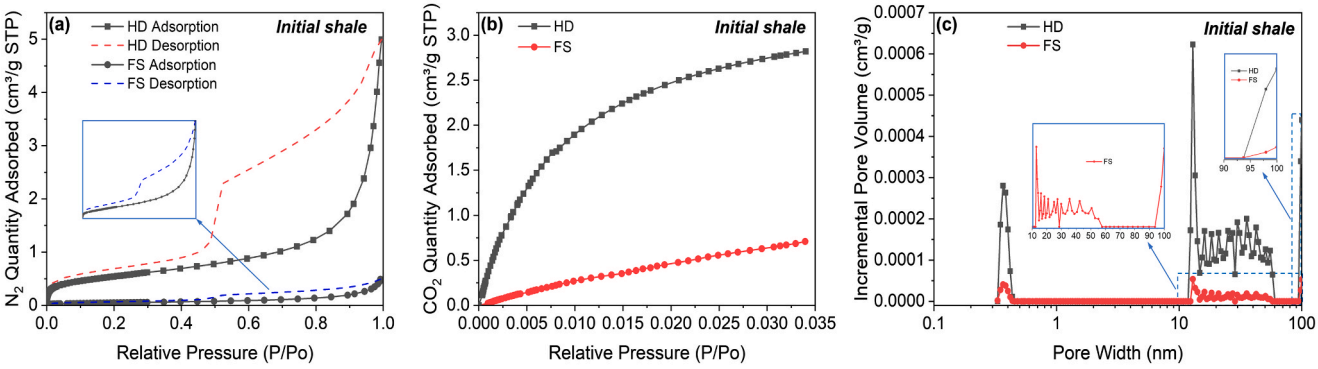

Fig. 2. N_2 and CO_2 sorption isotherms for initial HD and FS shales. (a) N_2 sorption isotherm, (b) CO_2 adsorption isotherm, and (c) Distribution of pore volume with pore width derived from CO_2 and N_2 isotherms.

Table 1
Pore structure characteristics of HD and FS samples.

Sample	Experiment		BET surface area[a] (m^2/g)	V_{ultra}[b] (cm^3/g)	V_{micro}[c] (cm^3/g)	V_{meso}[d] (cm^3/g)	V_{total}[e] (cm^3/g)	D[f] (nm)	W[g] (nm)
HD	Initial		1.96	0.0010	0.0010	0.0057	0.0071	14.48	15.21
	NP	Stage 1	0.07	0.0003	0.0003	0.0001	0.0005	31.56	40.67
		Stage 2	0.53	0.0005	0.0005	0.0008	0.0017	12.97	14.84
		Stage 3	2.76	0.0006	0.0006	0.0131	0.0191	27.65	28.99
		Stage 4	6.94	0.0011	0.0011	0.0270	0.0366	21.06	20.98
	LP	Stage 1	3.06	0.00046	0.00046	0.0193	0.0230	30.09	31.14
		Stage 2	10.38	0.00013	0.00013	0.0698	0.0831	32.01	33.25
		Stage 3	15.96	0.00001	0.00033	0.0885	0.1153	28.91	31.06
		Stage 4	26.27	0.00267	0.00323	0.1069	0.1349	20.55	21.39
	HP	Stage 1	3.25	0.00044	0.00044	0.0197	0.0236	28.94	30.06
		Stage 2	8.89	0.00033	0.00033	0.0578	0.0743	33.42	34.97
		Stage 3	23.55	0.00000	0.00011	0.1312	0.1672	28.40	30.52
		Stage 4	46.36	0.00224	0.00653	0.1557	0.2020	17.43	18.50
FS	Initial		0.19	0.0001	0.0001	0.0004	0.0007	14.34	15.62
	NP	Stage 1	0.03	0.00004	0.00004	0.0003	0.0004	63.88	76.05
		Stage 2	0.78	0.00024	0.00024	0.0033	0.0056	28.64	30.60
		Stage 3	2.90	0.00021	0.00021	0.0176	0.0221	30.41	31.58
		Stage 4	4.68	0.00055	0.00055	0.0229	0.0276	23.59	24.11
	LP	Stage 1	0.80	0.0003	0.0003	0.0033	0.0047	23.32	26.88
		Stage 2	3.35	0.0005	0.0005	0.0181	0.0229	27.32	28.70
		Stage 3	12.65	0.0015	0.0015	0.05	0.0547	17.31	17.56
		Stage 4	27.55	0.0036	0.0058	0.0649	0.0810	11.75	11.63
	HP	Stage 1	2.09	0.00048	0.00048	0.0083	0.0088	16.87	22.28
		Stage 2	4.34	0.00042	0.00042	0.0233	0.0291	26.87	26.95
		Stage 3	17.59	0.00154	0.00154	0.0686	0.0772	17.55	17.49
		Stage 4	46.28	0.00415	0.01006	0.0872	0.1059	9.15	9.22

[a] BET surface area = BET surface area model applied between 0.05–0.20P/P_o.
[b] V_{ultra} = ultra micropore volume (<0.8 nm) from non-local density functional theory carbon slit pore model.
[c] V_{micro} = volume of micro pores (<2 nm) from non-local density functional theory carbon slit pore model.
[d] V_{meso} = volume of mesopores (2–50 nm) from non-local density functional theory carbon slit pore model.
[e] V_{total} = total pore volume (up to 100 nm) from non-local density functional theory carbon slit pore model.
[f] D = average pore diameter (adsorption) using $4V_{tot}$/BET surface area.
[g] W = average window pore diameter (desorption) using $4V_{tot\_desorption}$/BET surface area.

trajectory, mineral reactions, particularly carbonate dissolution and clay collapse, critically modulate porosity, and water together with pressure act as synergistic environmental modifiers. To elucidate this framework, we first examine how thermal maturity, the fundamental driver of porosity, manifests differently under varying pyrolysis conditions and between shales.

The strong positive correlation between nitrogen adsorption capacity and VR across all conditions confirms thermal maturity as the fundamental driver of pore development (Fig. 5), consistent with previous studies [8–10,56,57]. However, critical nuances emerge. The correlation is significantly stronger under hydrous pyrolysis (LP, HP) when data from initial immaturity are included, whereas a comparable fit under NP conditions requires the exclusion of initial low-maturity data. This distinction suggests that hydrous pyrolysis provides a more geologically realistic simulation. Furthermore, under hydrous conditions, FS shale with Type I kerogen and low TOC exhibited a tighter correlation than HD shale (Type II, high TOC), indicating a more efficient, predictable, and closely coupled relationship between pore development and hydrocarbon expulsion in the former.

Further evidence for kerogen-specific pathways is provided by TOC-normalized pore volume and surface area data (Fig. 6). The consistently higher normalized values in FS shale highlight the superior pore development efficiency of Type I kerogen, whose aliphatic structure leads to a higher yield of mobile hydrocarbons during primary cracking, facilitating efficient expulsion and leaving behind a more porous and rigid pyrobitumen network. In contrast, Type II kerogen (HD) may generate more polar compounds and asphaltenes that are more prone to pore-filling. This underscores why generalized maturity-porosity models often fail to predict reservoir quality across different shale systems.

To elucidate the role of organic conversion, we employed a mass-balance approach that compares measured pore volumes with theoretical values calculated from TOC loss and retention, representing the maximum potential pore space liberated from the organic matrix (Supplementary Note 1, Table S3, and Fig. 7). In this model, TOC loss corresponds to carbon converted into expelled mobile hydrocarbons, while retained TOC (primarily as bitumen) is associated with the creation of shrinkage pores [35].

The general congruence between calculated and measured trends confirms that TOC loss and retention is a primary driver of porosity generation. However, the notable discrepancies observed between the two values demonstrate that TOC loss and retention alone is insufficient and highlight the control exerted by additional compositional and environmental factors [10,35,58]. For HD shale, calculated pore volumes exceed measured values by ~ 86% under NP and by ~ 23% under LP and HP in Phase III, although measured values temporarily surpass calculated ones during early stages under hydrous conditions (Fig. 7). Similarly, FS shale exhibits lower measured than calculated pore volume under NP. Under hydrous conditions, however, its measured pore volume exceeds the calculated value, especially in Phase III, where it is 20–26% higher (Fig. 7e-f, Supplementary Note 2).

The lower measured pore volume under NP conditions is primarily attributed to pore-throat blockage by retained bitumen and pyrobitumen [59–61]. Direct evidence for this mechanism includes elevated retained bitumen content (Table S2), high pre-extraction S_1 values, and significant post-extraction TOC (Table S4). Such blockage isolates pores, rendering them inaccessible to gas adsorption measurements [41]. This finding is consistent with micro-CT studies, which report that a substantial fraction of shale porosity, particularly organic-hosted porosity, exists as isolated or poorly connected clusters [62–67]. Our SEM images (Fig. 8) provide direct visual confirmation of pervasive bitumen/pyrobitumen-coated surfaces, creating the blocked and isolated pore systems that explain the discrepancy between measured and calculated

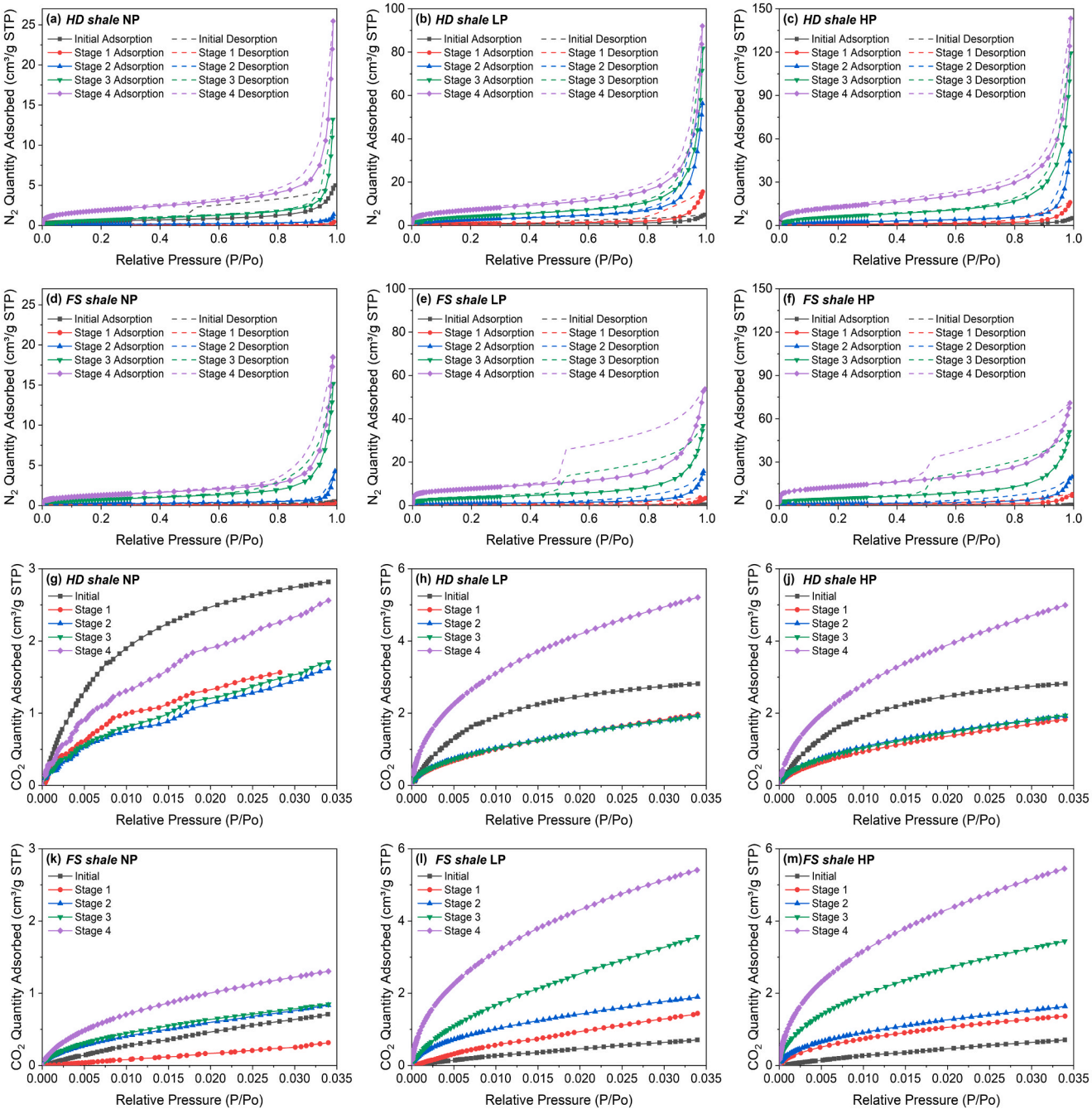

Fig. 3. N_2 and CO_2 sorption isotherms of sequentially pyrolyzed HD and FS shales. (a-f) N_2 sorption isotherms: (a) NP of HD shale, (b) LP of HD shale, (c) HP of HD shale, (d) NP of FS shale, (e) LP of FS shale, and (f) HP of FS shale; (g-m) CO_2 sorption isotherms: (g) NP of HD shale, (h) LP of HD shale, (j) HP of HD shale, (k) NP of FS shale, (l) LP of FS shale, and (m) HP of FS shale.

pore volumes, particularly in HD samples (Fig. 8a–b). These occlusive effects dominate under NP, but are mitigated under hydrous conditions (Fig. 8c, 8f), where measured pore volumes match or even exceed calculated values in Phases I–II (Fig. 7b, c, e, f) due to the combined effects of water, water pressure, and mineral-related contributions. The bitumen/pyrobitumen infilling effect exhibited a mild manifestation in the FS samples (Fig. 8).

Beyond its chemical role in hydrocarbon generation, water fundamentally regulates pore architecture by shifting the regime from pore-filling to pore-enhancement [38]. Water introduces hydrogen ions that promote hydrocarbon formation [68] and, through its solvation capacity, facilitates the dissociation of organic macromolecules from mineral, mitigating pore-filling [39,40,58]. While hydrous conditions (LP/HP) consistently enhance porosity compared to NP, increasing water pressure beyond LP yields only marginal gains in Phase I (Fig. 6), indicating that water presence is the dominant control during this phase.

Pressure exerts dual and competing influences. External confining pressure compacts the pore system [36,69], while internal pore pressure from hydrocarbon formation and pore-water expansion counteracts this effect [35,70,71]. Our data confirm the dominance of internal pressure in closed hydrous systems, as evidenced by increasing pore volumes from NP to LP (Fig. 6). High internal pressure can induce bitumen "swelling" [72–74], influencing whether bitumen is expelled (pore-forming) or retained and solidified (pore-plugging), and promoting secondary pore space upon its later cracking or expulsion [35]. The balance between internal pore and external pressures controls nanopore

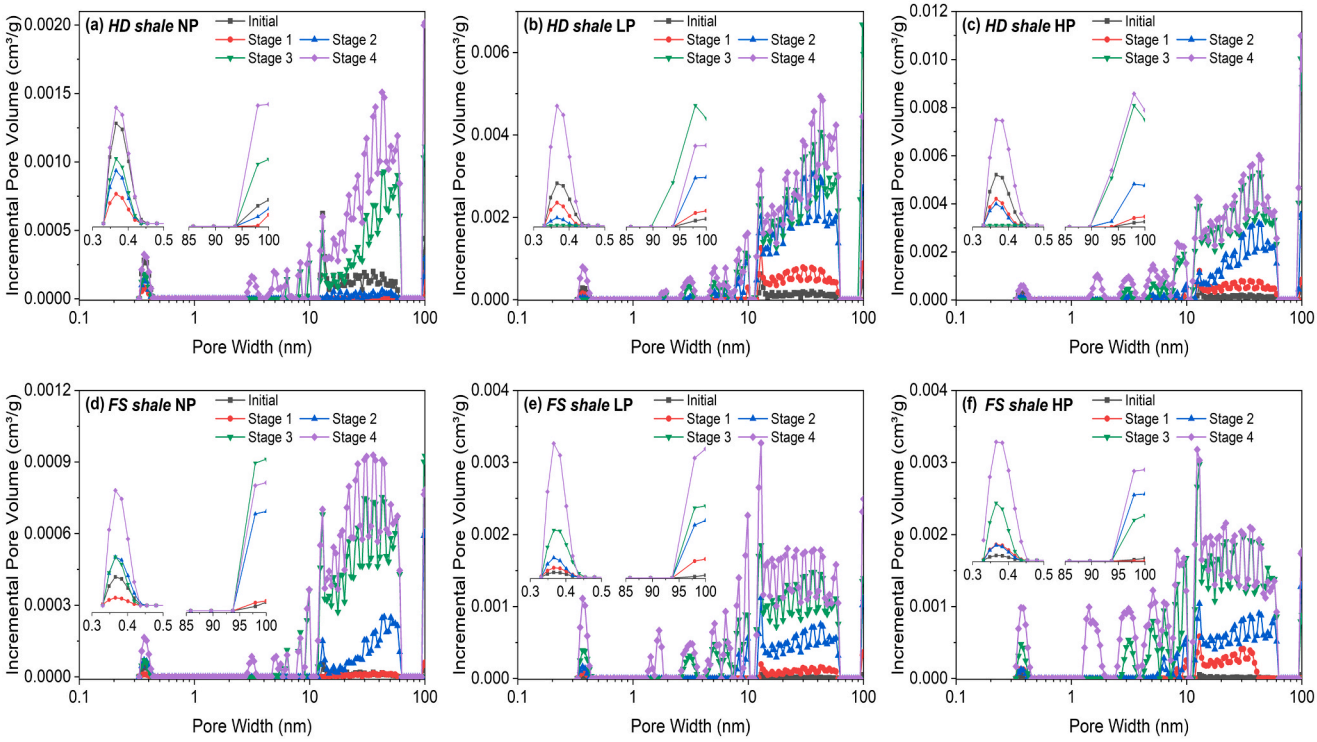

Fig. 4. Distribution of pore volume with pore width derived from CO_2 and N_2 isotherms of pyrolyzed rocks. (a) NP of HD shale, (b) LP of HD shale, (c) HP of HD shale, (d) NP of FS shale, (e) LP of FS shale, and (f) HP of FS shale.

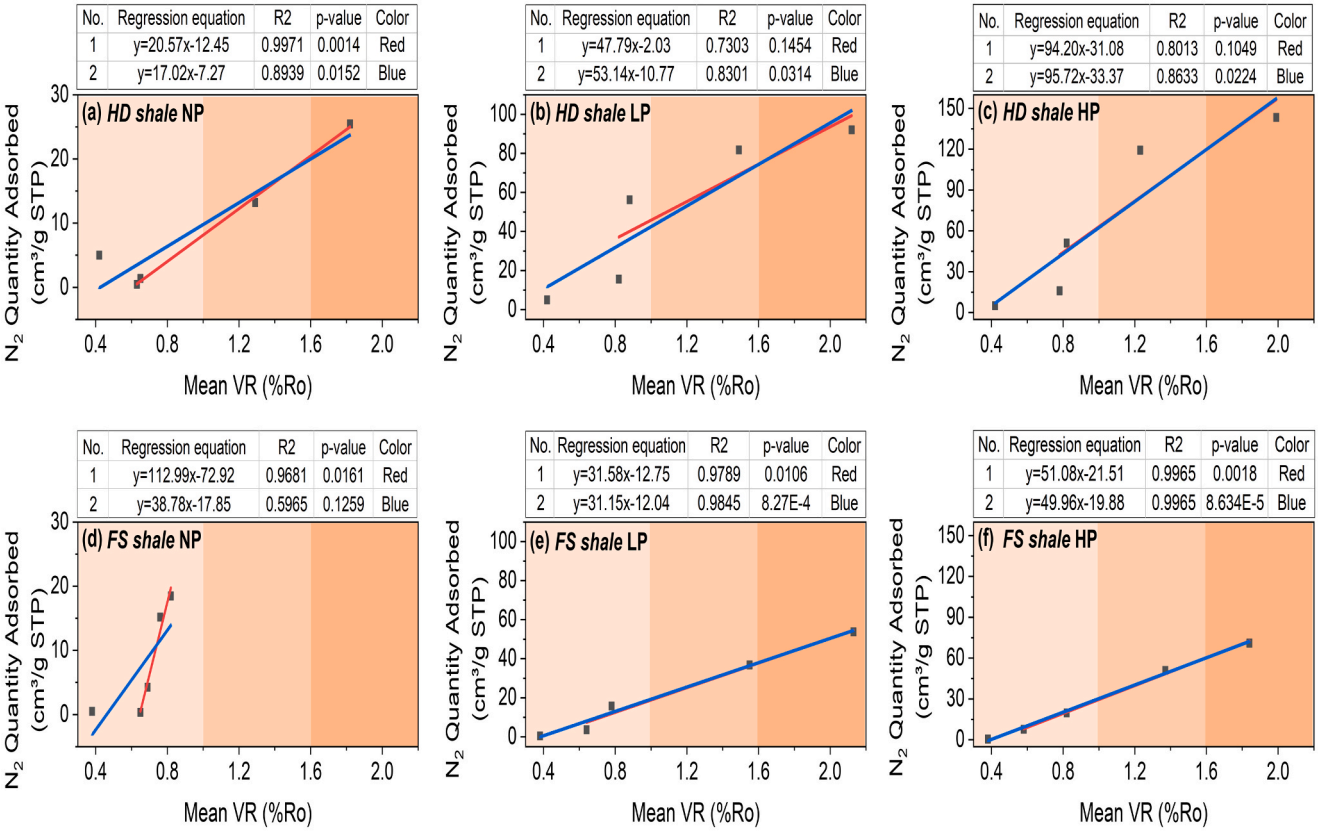

Fig. 5. Relationship between nitrogen adsorption capacity and thermal maturity of samples. (a) NP of HD shale, (b) LP of HD shale, (c) HP of HD shale, (d) NP of FS shale, (e) LP of FS shale, and (f) HP of FS shale (Note: Blue lines represent fitting curves including initial shale values, while red lines denote curves excluding initial shale value; Light-to-dark background color transitions correspond to Phase I, Phase II, and Phase III of the organic matter evolution process, respectively). (For interpretation of the references to colour in this figure legend, the reader is referred to the web version of this article.)

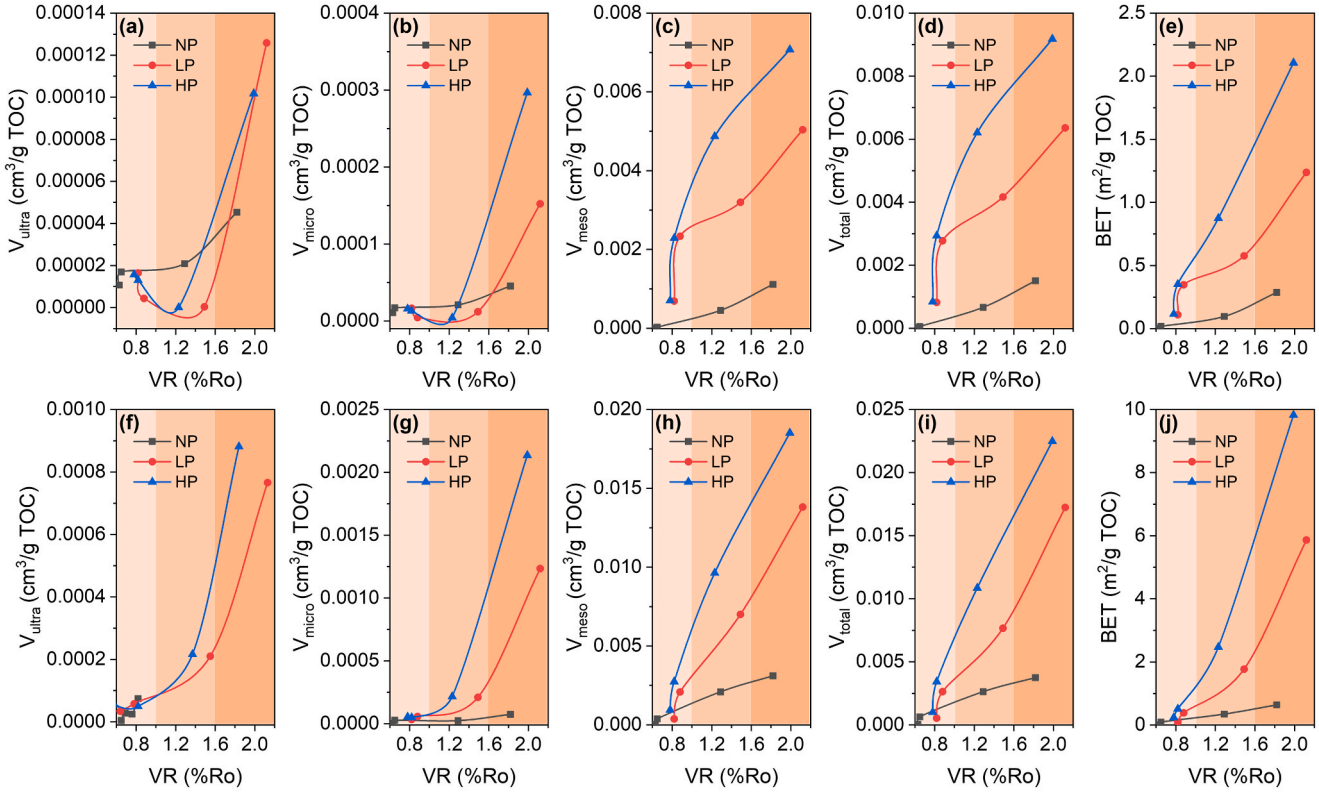

Fig. 6. TOC-normalized pore volumes and BETs of HD and FS samples. (a) HD ultra-micropore volume, (b) HD micropores volume, (c) HD mesopore volume, (d) HD total pore volume, (e) HD BET surface area, (f) FS ultra-micropore volume, (g) FS micropores volume, (h) FS mesopore volume, (i) FS total pore volume, and (j) FS BET surface area (Note: Light-to-dark background color transitions correspond to Phase I, Phase II, and Phase III of the organic matter evolution process, respectively).

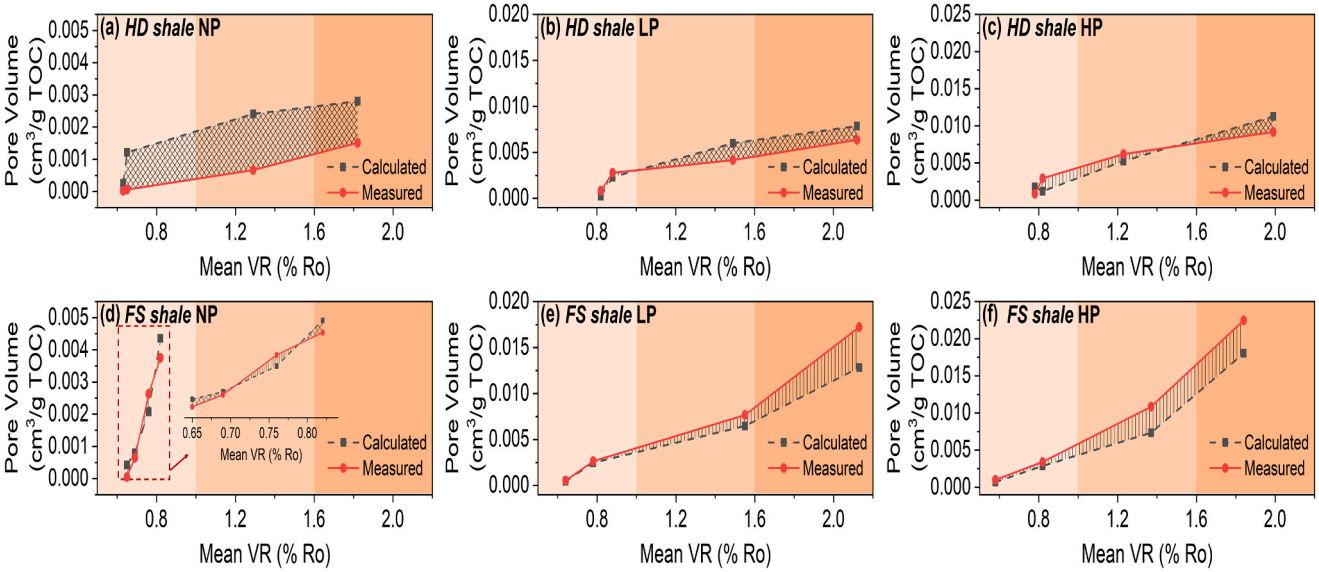

Fig. 7. Comparison of TOC-normalized measured and calculated total pore volumes. (a) NP of HD shale, (b) LP of HD shale, (c) HP of HD shale, (d) NP of FS shale, (e) LP of FS shale, and (f) HP of FS shale (Note: Light-to-dark background color transitions correspond to Phase I, Phase II, and Phase III of the organic matter evolution process, respectively).

preservation, with internal pore pressure being more dominant [75].

Water amplifies internal pore pressure by enhancing hydrocarbon generation [68], raising pore-water pressure [75], and promoting carbonate dissolution, the latter accelerated by CO_2 from hydrous pyrolysis (i.e., $CaCO_3 + CO_2 + H_2O \rightarrow Ca^{2+} + 2HCO_3^-$) (Table S2), which creates acidic conditions conducive to secondary inorganic porosity [47,58]. Collectively, these mechanisms underscore that water presence, supported by pressure, is a more decisive factor in porosity evolution than pressure alone.

Under LP and HP, the lower measured pore volume of HD at high thermal maturity is attributed to the collapse of the I/S mixed-layer clay-rich matrix framework [76–78]. This interpretation is corroborated by

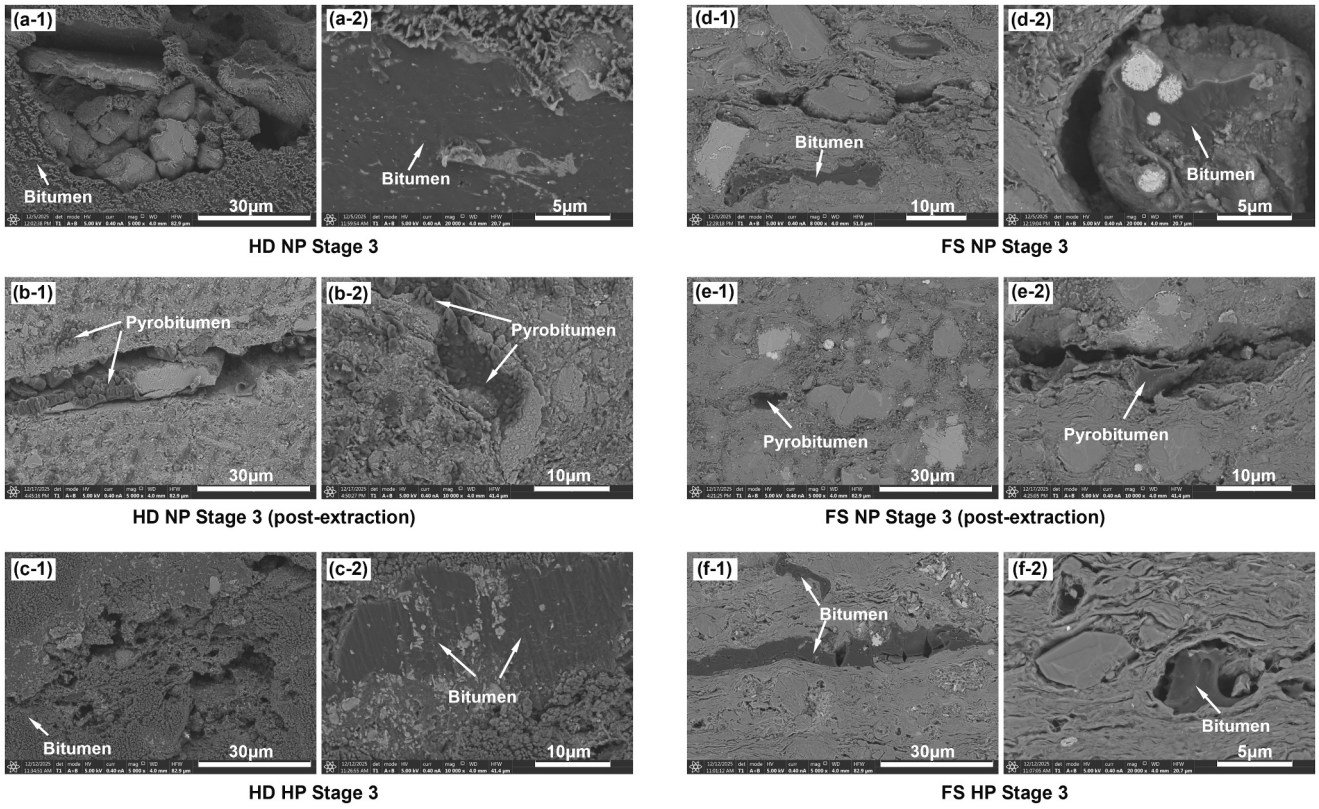

Fig. 8. SEM images of HD and FS samples. (a) HD NP Stage 3, (b) HD NP Stage 3 after extraction, (c) HD HP Stage 3, (d) FS NP Stage 3, (e) FS NP Stage 3 after extraction, and (f) FS HP Stage 3.

micro-CT studies, which reveal that clay mineral decomposition disrupts the layered structure and induces the collapse of larger pores, thereby reorganizing the pore network and reducing overall pore volume [20]. The transition equilibrium "crossover point" between calculated and measured values shifts from Phase I to Phase II (Fig. 7), which is due to water pressure. In contrast, the FS sample exhibits a net pore-volume increase during Phase III. Early-stage pore enhancement in FS shale is partly due to siderite decomposition, evidenced by CO_2 mainly released in Stage 1 (Table S2), whereas the Phase III porosity growth is predominantly attributed to the well-connected organic pores resulting from efficient hydrocarbon expulsion [43]. This highlights the inherently superior pore-preserving capability of Type I kerogen systems under favorable hydrous conditions.

Building upon the established roles of thermal maturity, organic and inorganic composition, and hydro-mechanical conditions, we synthesize a phase-specific model for nanopore evolution, as summarized in Fig. 9.

During Phase I (oil generation), the early generation of polar and high-viscosity bitumen leads to pore-throat blockage. Under hydrous conditions, this is mitigated by enhanced bitumen expulsion, while internal overpressure and mineral reactions promote micro-fracture development, resulting in minimal divergence between calculated and measured pore volumes (Fig. 7).

As maturation advances into Phase II (oil cracking), pore evolution is governed by a competition between exacerbated pore occlusion by bitumen and enhanced pore development from rising internal pressure. Water critically shifts this balance toward net pore formation by improving bitumen mobility and expulsion.

A clear divergence occurs in Phase III (gas cracking). FS shale (Type I) exhibits superior pore preservation and well-connected organic-hosted pores, a legacy of efficient hydrocarbon expulsion. In contrast, HD shale (Type II) suffers substantial porosity destruction due to the collapse of its I/S mixed-layer clay-rich matrix, compounded by earlier pore-filling by pyrobitumen.

Throughout, water is the paramount environmental moderator, reducing porosity destruction in HD shale while enhancing it in FS shale. Increasing water pressure (HP vs. LP) exhibits a secondary and composition-dependent effect, confirming that the benefits of elevated pressure are contingent upon specific geomechanical and geochemical context.

While this laboratory-derived framework provides a mechanistic basis for predicting porosity evolution, its direct application to geological settings requires consideration of inherent limitations. First, laboratory timescales cannot replicate million-year diagenetic processes, such as slow clay transformation kinetics. Second, natural shale systems are mineralogically and organically heterogeneous at multiple scales, whereas our study contrasts two end-member kerogen types. Real-world "sweet spot" prediction requires integrating these principles with local complexity. Third, our simplified experimental burial path does not capture the complex thermo-tectonic histories of natural basins, including episodes of heating, cooling, uplift, and fluctuating pressure regimes.

Therefore, this framework serves best as a conceptual guide. Effective exploration strategies should integrate their fundamental principles with detailed geological characterization. Future work should combine 3D pore-scale imaging (e.g., FIB-SEM, micro-CT) with basin modeling to bridge laboratory-derived mechanisms and reservoir-scale prediction.

5. Conclusions

This study provides a systematic, mechanistic framework for predicting pore evolution in organic-rich shales by decoupling the long-debated synergistic effects of thermal maturity, shale composition, water, and pressure. Our findings demonstrate that pore evolution is not merely a function of thermal maturity but is governed by a predictable hierarchy of controls. Shale composition sets the fundamental trajectory. Type I kerogen systems with stable mineral assemblages (e.g., FS

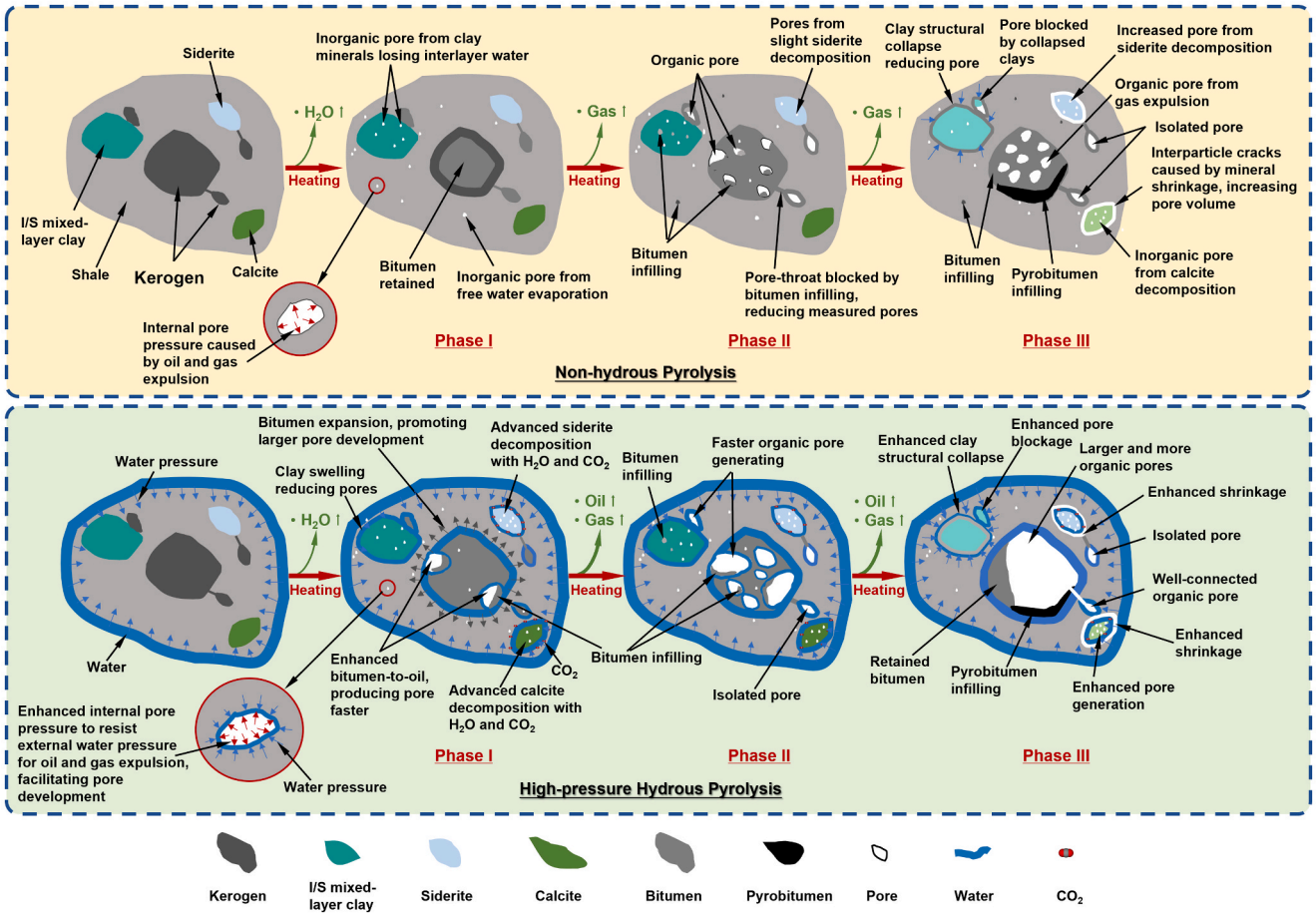

Fig. 9. Schematic diagram of the pore evolution in organic-rich shale during non-hydrous and high-pressure hydrous pyrolysis.

shale) achieve superior porosity via efficient hydrocarbon expulsion, whereas Type II kerogen systems with reactive clays (e.g., HD shale) suffer significant porosity reduction due to the combined pore-throat occlusion by retained bitumen/pyrobitumen and subsequent clay-framework collapse at high thermal maturity. Water is the paramount environmental modifier, whose presence, rather than its pressure magnitude, is critical for enhancing porosity by facilitating expulsion and mitigating pore-filling, especially during the early maturation stage. Pressure exerts a dual yet resolvable effect, with internally generated pore pressure promoting porosity and dominating over external compaction in closed generating systems. The most significant porosity enhancement occurs during the gas-cracking stage under synergistic water-pressure conditions.

This work shifts the research paradigm from viewing porosity as a simple maturity indicator, and establishes an integrated shale-water-pressure framework beyond traditional maturity-centric models. But its successful application for shale gas/oil "sweet spot" prediction requires calibration with basin-specific geological factors.

CRediT authorship contribution statement

Fengtian Bai: Writing – original draft, Investigation, Funding acquisition, Data curation, Conceptualization. **Lee A. Stevens:** Writing – review & editing, Supervision, Methodology, Investigation. **Clement N. Uguna:** Writing – review & editing, Supervision, Methodology, Investigation, Conceptualization. **Wei Li:** Writing – review & editing, Investigation. **Will Meredith:** Writing – review & editing, Supervision. **Colin E. Snape:** Supervision, Funding acquisition. **Christopher H. Vane:** Writing – review & editing, Methodology. **Yumin Liu:** Writing – review & editing. **Chenggong Sun:** Writing – review & editing, Supervision, Funding acquisition.

Declaration of competing interest

The authors declare that they have no known competing financial interests or personal relationships that could have appeared to influence the work reported in this paper.

Acknowledgments

This work was supported by the National Natural Science Foundation of China (Grant No. 42202344), Project of the Education Department of Jilin Province (Grant No. JJKH20250129KJ), and the Science and Technology Development Plan of Jilin Province (Grant No. 20250102102JC).

Appendix A. Supplementary data

Supplementary data to this article can be found online at https://doi.org/10.1016/j.fuel.2026.138559.

Data availability

Data will be made available on request.

The data that support the findings of this study are available within the Article and its Supplementary Information. Source data are available from the corresponding author upon reasonable request.

References

[1] Liu W, Xiao X, Gao P, Zhao Y, Xing Y, Fan Q, et al. Nanopore characteristics of lower Cambrian shale based on gas adsorption and multifractal analysis: implications for gas development and CO_2 storage. Fuel 2026;406:137047.
[2] Zhang T, Guo J, Zeng F, Zeng J, Lu C, Zhao Z. Gas mass transfer characteristics in shales: insights from multiple flow mechanisms, effective viscosity, and poromechanics. Gas Sci Eng 2024;125:205319.
[3] Babatunde K, Emami-Meybodi H. Gas transport in shales with applications to geological storage of H_2 and CO_2. Gas Sci Eng 2025;135:205550.
[4] Chen S, Li X, Zhu G, Lu Z, Wang R, Huang Y, et al. Classification, controlling factors, and multi-scale characterization techniques in shale reservoir pores: a comprehensive review. Gas Sci Eng 2025;140:205662.
[5] Muther T, Qureshi HA, Syed FI, Aziz H, Siyal A, Dahaghi AK, et al. Unconventional hydrocarbon resources: geological statistics, petrophysical characterization, and field development strategies. J Pet Explor Prod Technol 2022;12(6):1463–88.
[6] Jia C-Z, Pang X-Q, Song Y. Whole petroleum system and ordered distribution pattern of conventional and unconventional oil and gas reservoirs. Pet Sci 2023;20 (1):1–19.
[7] Yuan G, Cao Y, Jin Z, Schulz H-M, Jin Z, Fang R, et al. Thermally driven organic-inorganic interactions in sedimentary basins: a review from source rocks to reservoirs. Earth Sci Rev 2025;262:105043.
[8] Valenza II JJ, Drenzek N, Marques F, Pagels M, Mastalerz M. Geochemical controls on shale microstructure. Geology 2013;41(5):611–4.
[9] Modica CJ, Lapierre SG. Estimation of kerogen porosity in source rocks as a function of thermal transformation: example from the Mowry Shale in the Powder River Basin of Wyoming. AAPG Bull 2012;96(1):87–108.
[10] Chen J, Xiao XM. Evolution of nanoporosity in organic-rich shales during thermal maturation. Fuel 2014;129:173–81.
[11] Ross DJK, Marc BR. The importance of shale composition and pore structure upon gas storage potential of shale gas reservoirs. Mar Pet Geol 2009;26(6):916–27.
[12] Wang Y, Zhang T, Zhu Y, Chen S, Chang Z, Dou K, et al. Evolution of the molecular structure of kerogen in high to overmatured shale and its micropore response mechanism. Fuel 2025;393:134981.
[13] Wang D, Hu H, Wang T, Tang T, Li W, Zhu G, et al. Difference between of coal and shale pore structural characters based on gas adsorption experiment and multifractal analysis. Fuel 2024;371:132044.
[14] Dang ST, Sondergeld CH, Rai CS. Interpretation of nuclear-magnetic-resonance response to hydrocarbons: application to miscible enhanced-oil-recovery experiments in shales. SPE Reserv Eval Eng 2018;22(01):302–9.
[15] Sun L, Tuo J, Zhang M, Wu C, Wang Z, Zheng Y. Formation and development of the pore structure in Chang 7 member oil-shale from Ordos Basin during organic matter evolution induced by hydrous pyrolysis. Fuel 2015;158(1):549–57.
[16] Bai FT, Sun YH, Liu YM, Guo MY. Evaluation of the porous structure of Huadian oil shale during pyrolysis using multiple approaches. Fuel 2017;187:1–8.
[17] Zeng J, Jia W, Pa P, Guan C, Zhou C, Yuan X, et al. Composition and pore characteristics of black shales from the Ediacaran Lantian Formation in the Yangtze Block, South China. Mar Pet Geol 2016;76:246–61.
[18] Wang Q, Hu Q, Zhao C, Zhang C, Ilavsky J, Yu L, et al. Integrated experimental studies of pore structure and fluid uptake in the Bossier Shale in eastern Texas, USA. Fuel 2025;384:133926.
[19] Song Z, Zhang J, Jin S, Liu C, Abula A, Hou J, et al. The occurrences and mobility of shale oil in the pore space of terrestrial shale. Fuel 2024;374:132377.
[20] Zhu C-F, Zhang T-L, Pan J-F, Li Y-W, Sheng JJ, Ge D, et al. Evolution of the 3D pore structure of organic-rich shale with temperature based on micro-nano CT. Pet Sci 2025;22(6):2339–52.
[21] Wang Y, Jin Z. Effect of pore size distribution on hydrocarbon mixtures adsorption in shale nanoporous media from engineering density functional theory. Fuel 2019; 254:115650.
[22] Wan T, Chen S, Wu X, Chen G, Zhang X. An investigation on the pyrolysis of low-maturity organic shale by different high temperature fluids heating. Fuel 2024;374: 132498.
[23] Michels R, Landais P, Philp R, Torkelson B. Effects of pressure on organic matter maturation during confined pyrolysis of Woodford kerogen. Energy Fuel 1994;8 (3):741–54.
[24] Freund H, Clouse JA, Otten GA. Effect of pressure on the kinetics of kerogen pyrolysis. Energy Fuel 1993;7(6):1088–94.
[25] Knauss KG, Copenhaver SA, Braun LR, Burnham AK. Hydrous pyrolysis of New Albany and Phosphoria Shales: production kinetics of carboxylic acids and light hydrocarbons and interactions between the inorganic and organic chemical systems. Org Geochem 1997;27(7/8):477–96.
[26] Tissot B, Welte D. Petroleum Formation and Occurrence, second revised and enlarged version. Berlin: Springer; 1984.
[27] Braun RL, Burnham AK. Mathematical model of oil generation, degradation, and expulsion. Energy Fuel 1990;4(2):132–46.
[28] Tao W, Zou YR, Carr A, Liu JZ, Peng PA. Study of the influence of pressure on enhanced gaseous hydrocarbon yield under high pressure–high temperature coal pyrolysis. Fuel 2010;89(11):3590–7.
[29] Shuai Y, Pa P, Zou Y. Influence of pressure on stable carbon isotope ratio and production yield of coal-derived methane. Fuel 2006;85(5):860–6.
[30] Landais P, Michels R, Elie M. Are time and temperature the only constraints to the simulation of organic matter maturation? Org Geochem 1994;22(3–5):617–30.
[31] Price LC, Wenger LM. The influence of pressure on petroleum generation and maturation as suggested by aqueous pyrolysis. Org Geochem 1992;19(1):141–59.
[32] Zhonghong C, Zunjing M, Ming Z, Xiaoyu S, Shouchun Z, Youshu B. The effects of high pressure on oil-to-gas cracking during laboratory simulation experiments. J Pet Geol 2014;37(2):143–62.
[33] Uguna CN, Carr AD, Snape CE, Meredith W, Scotchman IC, Murray A, et al. Impact of high water pressure on oil generation and maturation in Kimmeridge clay and monterey source rocks: implications for petroleum retention and gas generation in shale gas systems. Mar Pet Geol 2016;73:72–85.
[34] Liu Y, Xiong Y, Li Y, Pa P. Effects of oil expulsion and pressure on nanopore development in highly mature shale: evidence from a pyrolysis study of the Eocene Maoming oil shale, south China. Mar Pet Geol 2017;86:526–36.
[35] Guo H, Jia W, Pa P, Zeng J, He R. Evolution of organic matter and nanometer-scale pores in an artificially matured shale undergoing two distinct types of pyrolysis: a study of the Yanchang Shale with Type II kerogen. Org Geochem 2017;105:56–66.
[36] Wang J, Zhu C, Ma C, Liang Z, Li K, Zhai C, et al. Pore compaction and crack evolution of shale rock under high-speed impact loading and different confining pressures. Sci Rep 2025;15(1):6511.
[37] Wang Z, Liu D, Yao Y, Li P, Sun X, Feng D, et al. Occurrence state of deep coalbed methane: a study considering the co-evolution of stress and pore structure. Fuel 2026;407:137418.
[38] Liu B, Mohammadi M-R, Ma Z, Bai L, Wang L, Xu Y, et al. Evolution of porosity in kerogen type I during hydrous and anhydrous pyrolysis: experimental study, mechanistic understanding, and model development. Fuel 2023;338:127149.
[39] Lu Y, Wang Z, Kang Z, Li W, Yang D, Zhao Y. Comparative study on the pyrolysis behavior and pyrolysate characteristics of Fushun oil shale during anhydrous pyrolysis and sub/supercritical water pyrolysis. RSC Adv 2022;12(26):16329–41.
[40] Liu K, Zhang Z, Safaei-Farouji M, Fattahi E, Zhang H, Liu B, et al. Quantifying pore structure heterogeneity of shale samples after solvent extraction following anhydrous and hydrous pyrolysis. Geoenergy Sci Eng 2024;239.
[41] Wang X, Zhang K, Jiang Z, Lin Y, Song Y, Jia C, et al. Hydrocarbon generation and pore evolution in marine organic-rich shales across maturation stages. Fuel 2025; 402:136050.
[42] Zou C, Dong D, Wang Y, Li X, Huang J, Wang S, et al. Shale gas in China: characteristics, challenges and prospects (II). Pet Explor Dev 2016;43(2):182–96.
[43] Bai F, Uguna CN, Meredith W, Snape CE, Vane CH, Sun C. Thermal evolution and hydrocarbon generation of organic matter in shales via sequential high-pressure hydrous pyrolysis: implications for in-situ conversion of unconventional resource. Fuel Process Technol 2025. 108327.
[44] Uguna CN, Carr AD, Snape CE, Meredith W, Castro-Díaz M. A laboratory pyrolysis study to investigate the effect of water pressure on hydrocarbon generation and maturation of coals in geological basins. Org Geochem 2012;52:103–13.
[45] Uguna CN, Carr AD, Snape CE, Meredith W. High pressure water pyrolysis of coal to evaluate the role of pressure on hydrocarbon generation and source rock maturation at high maturities under geological conditions. Org Geochem 2015;78: 44–51.
[46] Whitelaw P, Uguna CN, Stevens LA, Meredith W, Snape CE, Vane CH, et al. Shale gas reserve evaluation by laboratory pyrolysis and gas holding capacity consistent with field data. Nat Commun 2019;10(1):3654.
[47] Khairy A, Uguna CN, Vane CH, El Diasty WS, Peters KE, Snape CE, et al. The effect of high pressure on hydrocarbon generation from Type-I kerogen source rocks: Implications for petroleum system evolution. Int J Coal Geol 2025;300:104708.
[48] Li W, Stevens LA, Uguna CN, Vane CH, Meredith W, Tang L, et al. Comparison of the impact of moisture on methane adsorption and nanoporosity for over mature shales and their kerogens. Int J Coal Geol 2021;237:103705.
[49] Brunauer S, Emmett PH, Teller E. Adsorption of gases in multimolecular layers. J Am Chem Soc 1938;60(2):309–19.
[50] Thommes M, Kaneko K, Neimark AV, Olivier JP, Rodriguez-Reinoso F, Rouquerol J, et al. Physisorption of gases, with special reference to the evaluation of surface area and pore size distribution (IUPAC Technical Report). Pure Appl Chem 2015;87(9–10):1051–69.
[51] Rexer TFT, Benham MJ, Aplin AC, Thomas KM. Methane adsorption on shale under simulated geological temperature and pressure conditions. Energy Fuel 2013;27 (6):3099–109.
[52] Rouquerol J, Llewellyn P, Rouquerol F. Is the bet equation applicable to microporous adsorbents? In: Llewellyn PL, Rodriquez-Reinoso F, Rouqerol J, Seaton N, editors. Studies in Surface Science and Catalysis. Elsevier; 2007. p. 49–56.
[53] Qi L, Tang X, Wang Z, Peng X. Pore characterization of different types of coal from coal and gas outburst disaster sites using low temperature nitrogen adsorption approach. Int J Min Sci Technol 2017;27(2):371–7.
[54] Bai F, Uguna CN, Meredith W, Snape CE, Vane CH, Sun C. Thermal evolution and hydrocarbon generation of organic matter in shales via sequential high-pressure hydrous pyrolysis: Implications for in-situ conversion of unconventional resource. Fuel Process Technol 2025;278:108327.
[55] Sing KSW, Everett DH, Haul RAW, Moscou L, Pierotti RA, Rouquerol J, et al. Reporting physisorption data for gas/solid systems with special reference to the determination of surface area and porosity (Recommendations 1984). Pure Appl Chem 1985;57:603–19.
[56] Löhr SC, Baruch ET, Hall PA, Kennedy MJ. Is organic pore development in gas shales influenced by the primary porosity and structure of thermally immature organic matter? Org Geochem 2015;87:119–32.
[57] Pommer M, Milliken K. Pore types and pore-size distributions across thermal maturity, Eagle Ford Formation, southern Texas. AAPG Bull 2015;99(9):1713–44.
[58] Mathia EJ, Bowen L, Thomas KM, Aplin AC. Evolution of porosity and pore types in organic-rich, calcareous, Lower Toarcian Posidonia Shale. Mar Pet Geol 2016;75: 117–39.

[59] Mastalerz M, Schimmelmann A, Drobniak A, Chen Y. Porosity of Devonian and Mississippian New Albany Shale across a maturation gradient: insights from organic petrology, gas adsorption, and mercury intrusion. AAPG Bull 2013;97(10):1621–43.
[60] Wei L, Mastalerz M, Schimmelmann A, Chen Y. Influence of Soxhlet-extractable bitumen and oil on porosity in thermally maturing organic-rich shales. Int J Coal Geol 2014;132:38–50.
[61] Bernard S, Wirth R, Schreiber A, Schulz H-M, Horsfield B. Formation of nanoporous pyrobitumen residues during maturation of the Barnett Shale (Fort Worth Basin). Int J Coal Geol 2012;103:3–11.
[62] Zhang L, Zhao D, Yan K, Wang J, Fan L. Characterization of CT pore structure and permeability evolution of water-bearing coal samples under the effect of liquid nitrogen freeze–thaw cycle. Fuel 2026;404:136186.
[63] Lv W, Jin Z, Deng C, Wang Y, Mu Y. Investigation of pore-fracture evolution in pre-acidified coal under NMP treatment by CT scanning. Fuel 2026;404:136185.
[64] Liu Q, Sun M, Sun X, Liu B, Ostadhassan M, Huang W, et al. Pore network characterization of shale reservoirs through state-of-the-art X-ray computed tomography: a review. Gas Sci Eng 2023;113:204967.
[65] Saif T, Lin Q, Gao Y, Al-Khulaifi Y, Marone F, Hollis D, et al. 4D in situ synchrotron X-ray tomographic microscopy and laser-based heating study of oil shale pyrolysis. Appl Energy 2019;235:1468–75.
[66] Saif T, Lin Q, Butcher AR, Bijeljic B, Blunt MJ. Multi-scale multi-dimensional microstructure imaging of oil shale pyrolysis using X-ray micro-tomography, automated ultra-high resolution SEM, MAPS Mineralogy and FIB-SEM. Appl. Energy 2017;202:628–47.
[67] Wang K, Chandler M, Wang J, Dowey P, Storm M, Taylor KG, et al. Time-lapse nanometre-scale 3D synchrotron imaging and image-based modelling of the response of shales to heating. Int J Coal Geol 2021;244:103816.
[68] Lewan MD. Experiments on the role of water in petroleum formation. Geochim Cosmochim Acta 1997;61(17):3691–723.
[69] Ju Y-W, Hou X-G, Han K, Song Y, Xiao L, Huang C, et al. Experimental deformation of shales at elevated temperature and pressure: pore-crack system evolution and its effects on shale gas reservoirs. Pet Sci 2024;21(6):3754–73.
[70] Jia W, Wang Q, Liu J, Pa P, Li B, Lu J. The effect of oil expulsion or retention on further thermal degradation of kerogen at the high maturity stage: a pyrolysis study of type II kerogen from Pingliang shale, China. Organ. Geochem. 2014;71:17–29.
[71] Gai H, Xiao X, Cheng P, Tian H, Fu J. Gas generation of shale organic matter with different contents of residual oil based on a pyrolysis experiment. Org Geochem 2015;78:69–78.
[72] Svrcek WY, Mehrotra AK. Gas solubility, viscosity and density measurements for athabasca bitumen. J Can Pet Technol 1982;21.
[73] Yang C, Gu Y. A novel experimental technique for studying solvent mass transfer and oil swelling effect in the vapour extraction (VAPEX). Proc. J. Canad. Petrol. Technol. 2005;46(9).
[74] Yang C, Gu Y. Diffusion coefficients and oil swelling factors of carbon dioxide, methane, ethane, propane, and their mixtures in heavy oil. Fluid Phase Equilib 2006;243:64–73.
[75] Zhang S, Sang Q, Dong M. Experimental study of pressure sensitivity in shale rocks: effects of pore shape and gas slippage. J Nat Gas Sci Eng 2021;89:103885.
[76] Bai FT, Sun YH, Liu YM, Li Q, Guo MY. Thermal and kinetic characteristics of pyrolysis and combustion of three oil shales. Energ Conver Manage 2015;97:374–81.
[77] Neaman A, Pelletier M, Villieras F. The effects of exchanged cation, compression, heating and hydration on textural properties of bulk bentonite and its corresponding purified montmorillonite. Appl Clay Sci 2003;22(4):153–68.
[78] Noyan H, Önal M, Sarikaya Y. The effect of heating on the surface area, porosity and surface acidity of a bentonite. Clay Clay Miner 2006;54(3):375–81.